Energy Transport by Nonlinear Internal Waves

J. N. MOUM

College of Oceanic and Atmospheric Sciences, Oregon State University, Corvallis, Oregon

J. M. KLYMAK

University of Victoria, Victoria, British Columbia, Canada

J. D. NASH, A. PERLIN, AND W. D. SMYTH

College of Oceanic and Atmospheric Sciences, Oregon State University, Corvallis, Oregon

(Manuscript received 3 May 2006, in final form 13 November 2006)

ABSTRACT

Winter stratification on Oregon's continental shelf often produces a near-bottom layer of dense fluid that acts as an internal waveguide upon which nonlinear internal waves propagate. Shipboard profiling and bottom lander observations capture disturbances that exhibit properties of internal solitary waves, bores, and gravity currents. Wavelike pulses are highly turbulent (instantaneous bed stresses are 1 N m^{-2}), resuspending bottom sediments into the water column and raising them 30+ m above the seafloor. The wave cross-shelf transport of fluid often counters the time-averaged Ekman transport in the bottom boundary layer. In the nonlinear internal waves that were observed, the kinetic energy is roughly equal to the available potential energy and is $O(0.1)$ megajoules per meter of coastline. The energy transported by these waves includes a nonlinear advection term $\langle uE \rangle$ that is negligible in linear internal waves. Unlike linear internal waves, the pressure–velocity energy flux $\langle up \rangle$ includes important contributions from nonhydrostatic effects and surface displacement. It is found that, statistically, $\langle uE \rangle \simeq 2\langle up \rangle$. Vertical profiles through these waves of elevation indicate that $up(z)$ is more important in transporting energy near the seafloor while $uE(z)$ dominates farther from the bottom. With the wave speed c estimated from weakly nonlinear wave theory, it is verified experimentally that the total energy transported by the waves is $\langle up \rangle + \langle uE \rangle \simeq c\langle E \rangle$. The high but intermittent energy flux by the waves is, in an averaged sense, $O(100)$ watts per meter of coastline. This is similar to independent estimates of the shoreward energy flux in the semidiurnal internal tide at the shelf break.

1. Introduction

The circulation over Oregon's continental shelf is principally wind driven (Huyer et al. 1978). The large-scale cross-shelf circulation is thought to be determined by Ekman dynamics (Perlin et al. 2005a). Predominantly northerly winds in spring/summer drive near-surface fluid offshore, generating a cross-shelf density gradient that sustains a southward coastal jet, which in turn drives near-bottom fluid onshore. In fall/winter, winds are predominantly southerly, resulting in a northward coastal jet and effectively reversing the cross-shelf circulation pattern. As a consequence, there is a clear distinction in the cross-shelf structure of the stratification between upwelling and downwelling seasons (Fig. 1).

In spring and summer, stratification is concentrated near the surface. This provides a waveguide in which nonlinear internal waves of depression are commonly observed to propagate (Moum et al. 2003). In the left panel of Fig. 1 two examples of these are evident. At 20 km offshore a large-wavelength wave is seen propagating onshore at about 0.3 m s^{-1}; the leading edge of this wave appears to be borelike. A train of smaller-scale waves inshore at 1.5 km is aliased in our profiling ob-

Corresponding author address: J. N. Moum, College of Oceanic and Atmospheric Sciences, Oregon State University, COAS Admin. Bldg. 104, Corvallis, OR 97331-5503.
E-mail: moum@coas.oregonstate.edu

DOI: 10.1175/JPO3094.1

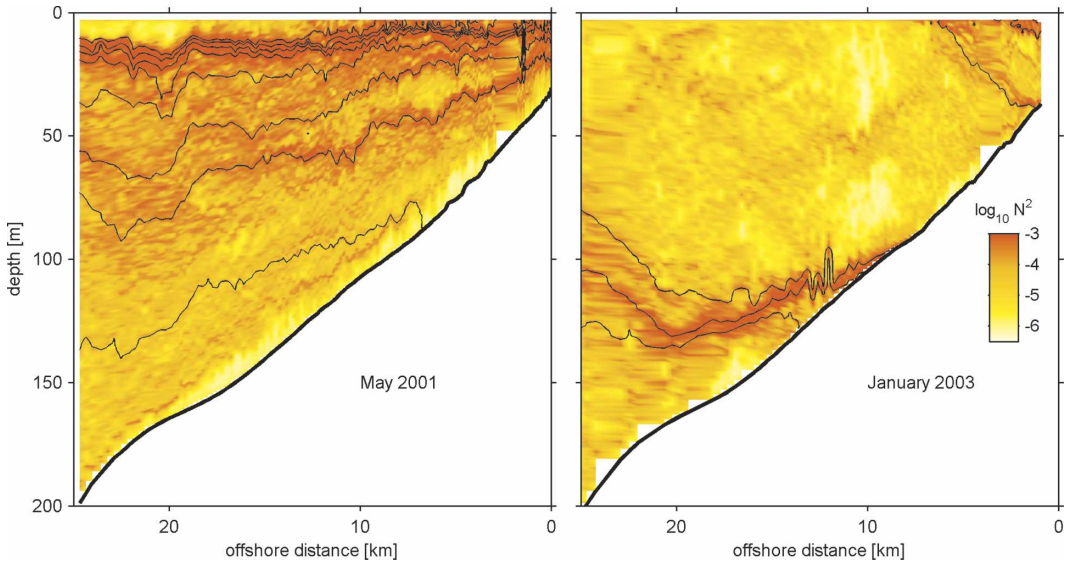

FIG. 1. Image plots of squared buoyancy frequency (red high; yellow low) from profiler measurements of density made across the Oregon shelf at 45°00′N in upwelling season (May 2001) and in downwelling season (January 2003). Contours of density are plotted at intervals of 0.5 kg m^{-3}. These cross-shore distributions were constructed from data obtained from 148 profiles in May 2001 and 202 profiles in January 2003. Each transect required approximately 8 h to execute. (left) Nonlinear internal waves of depression at 2 km, and (right) a large internal bore at 20 km. Nonlinear internal waves of elevation appear in the right-hand panel at 12 km.

servations. In both cases, the influence of the waves is clear throughout the water column.

In winter, the water column is typically weakly stratified, from the combination of wind-driven mixing, onshore transport of light near-surface fluid in the upper Ekman layer, and offshore transport of dense near-bottom fluid in the bottom Ekman layer. In the right panel of Fig. 1, the lightest fluid is trapped inshore of 6 km. At times, this combination of motions leaves the middle portion of the shelf completely unstratified. However, at other times, a thin stratified layer exists near the seafloor (Fig. 1, right panel) upon which nonlinear waves of elevation propagate onshore (Klymak and Moum 2003). This particular example (Fig. 1) shows a train of waves propagating onshore at 12 km. Net fluid transport by these waves counters the offshore bottom Ekman transport.

When and where the internal tide steepens, it is frequently found that a significant portion of the tidal energy goes to generation of a nonlinear internal wave field [see Helfrich and Melville (2006) for a recent review]. Since stratification is more typically strong near the surface and this is where most observations have taken place, the result that we typically observe is a surface-trapped wave field (Sandstrom and Elliott 1984; Holloway 1987; MacKinnon and Gregg 2003). When stratification is concentrated near the bottom, tidal and mesoscale energy can also generate a bottom-trapped nonlinear internal wave field (Klymak and Moum 2003; Hosegood and van Haren 2003) that is similar to the form of nonlinear internal waves observed in the atmosphere (Smith et al. 1982).

Quantification of the energy transport in nonlinear internal waves has been limited by the resolution of the available observations (Pinkel 2000; Klymak and Moum 2003; Lien et al. 2005; Klymak et al. 2006) or has been based on a linear formulation of the energy flux (Chang et al. 2006). An evaluation of nonlinear contributions to the wave energy transport has only recently been attempted from numerical simulations (Venayagamoorthy and Fringer 2005; Lamb 2007) and from observations obtained in nonlinear internal waves of depression (Scotti et al. 2006). To define the energy transport mechanisms in the waves requires velocity measurements with such detail that they are difficult to obtain from a moving ship. Our recent observations from a bottom lander fixed to the seafloor provide sufficient detail to fully evaluate the wave energy transport terms in nonlinear internal waves of elevation.

The prevalence of bottom-trapped nonlinear internal waves over the Oregon shelf in the winter downwelling season is evident from a set of observations made in January 2003. These include two sets of moored observations as well as shipboard profiling measurements both across the shelf and, for 36 h, at the location of the

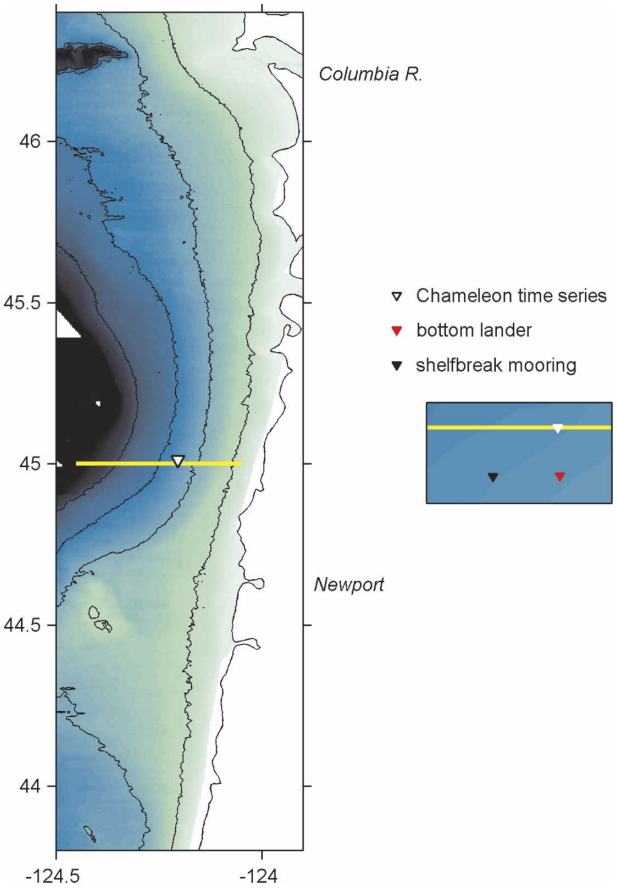

FIG. 2. Location of the experiment off the Oregon coast in January 2003. Cross-shelf range of repeated transects is shown in yellow. Location of 36-h time series is shown as a white triangle. Depths are contoured at 50, 100, 150, and 200 m. The inset shows relative locations of time series, bottom lander, and shelfbreak mooring. The lander is 653 m due east of the mooring and 850 m due south of the profiling time series. The mean water depth at lander and profiling station is 124 m; the depth at the location of the shelfbreak mooring is 5 m greater.

moorings (Fig. 2). These show both cross-shore structure and temporal evolution of the waves.

Our objective here is twofold: first, to provide a useful description of near-bottom flows over Oregon's continental shelf from a series of complementary observations and, second, to quantify how the energy in nonlinear internal waves is partitioned and transported. This wave energy is compared with the energy available in the internal tide. We begin with the development of a theoretical framework to describe the energetics (section 2). This is followed by a brief presentation of the measurements (section 3) and a description of the relevant observations (section 4). We then discuss how these observations are used to evaluate nonlinear internal wave energy and its transport (section 5) and conclude with a discussion of some of the consequences of these results (section 6) and a summary (section 7). Details of our estimates of turbulence kinetic energy dissipation rate from bottom lander measurements are outlined in the appendix.

2. Energetics: Theoretical framework

In this section, we define the wave kinetic energy, available potential energy, and the energy flux for a two-dimensional, nonhydrostatic, nonlinear internal wave. This results in an evolution equation for the wave energy that differs significantly from that which governs linear internal wave energetics (e.g., Kundu and Cohen 2004). Following Venayagamoorthy and Fringer (2005), we form an energy equation (J m^{-3}) from the sum of the dot product of the momentum equation with the velocity vector **u**, and $gz \times$ the mass conservation equation, where g is the acceleration due to gravity and density is

$$\rho(x, z, t) = \rho_o + \rho_b(z) + \rho_w(x, z, t). \tag{1}$$

The density is defined as the sum of a background density profile, $\rho_o + \rho_b(z)$, and a perturbation associated with the wave, $\rho_w(x, z, t)$.

Neglecting mixing, mass conservation becomes

$$\frac{\partial \rho_w}{\partial t} + u\frac{\partial \rho_w}{\partial x} + w\left(\frac{\partial \rho_b}{\partial z} + \frac{\partial \rho_w}{\partial z}\right) = 0. \tag{2}$$

The pressure disturbance in a nonlinear internal wave is derived by Moum and Smyth (2006) as the sum of internal hydrostatic pressure (due to isopycnal displacement) plus external hydrostatic pressure (due to surface displacement) plus nonhydrostatic pressure (due to vertical fluid accelerations),

$$p = g\int_z^H (\rho_o + \rho_b + \rho_w)\, dz' + \rho_o g\eta_H + p_{\rm nh}, \tag{3}$$

where $z = 0$ is the seafloor and $z = H$ the height of the undisturbed surface. Here, $\eta_H(x, t)$ is the surface displacement, the nonhydrostatic pressure

$$p_{\rm nh} = \rho_o \int_z^H \frac{Dw}{Dt}\, dz', \tag{4}$$

and we refer to the internal hydrostatic pressures [associated with the terms in the integrand of Eq. (3)] separately as p_h^o, p_h^b, and p_h^w.

We define the energy density (i.e., per unit volume) as

$$E = \text{KE} + \text{APE}, \tag{5}$$

where

$$\mathrm{KE} = \frac{1}{2}\rho_o u_i u_i. \tag{6}$$

The available potential energy is

$$\mathrm{APE} = \rho_w g z. \tag{7}$$

Here APE represents the potential energy due solely to the presence of the wave disturbance relative to the fluid at rest. This is the potential energy that is available from the disturbance for conversion to kinetic energy, including turbulence. Its definition has been clarified by Hebert (1988) for application to a general isolated disturbance and by Winters et al. (1995) for a turbulent flow. More recently, Lamb (2007) and Scotti et al. (2006) define the available potential energy for a nonlinear internal wave. In the case of linear waves, (7) reduces to $g^2\rho_w^2/2\rho_o N^2$ (Kundu and Cohen 2004).

The wave perturbation density, ρ_w, is defined by the requirement that the wave's APE be referenced to a thermodynamic rest state (Reid et al. 1981; Hebert 1988; Winters et al. 1995). We determined ρ_b by redistributing the observed density field to that rest state (resulting in horizontal isopycnals) over a distance of 50 wavelengths (L) of the observed wave. This is a sufficiently large area to ensure that the spatially averaged APE (i.e., $\int_{-25L}^{25L}\int_0^H [\mathrm{APE}]\, dz\, dx$) reaches an asymptote; ρ_w is then the difference between the observed density and ρ_b. This means that $\rho_w > 0$ in the vicinity of an elevation wave and $\rho_w < 0$, though small, elsewhere.[1]

The resultant energy equation is

$$\frac{\partial E}{\partial t} + \frac{\partial}{\partial x}[u(\mathrm{KE} + \mathrm{APE} + p_h^w + \rho_o g\eta_H + p_{\mathrm{nh}})] + \frac{\partial}{\partial z}[w(\mathrm{KE} + p_h^o + p_h^b + p_h^w + \rho_o g\eta_H + p_{\mathrm{nh}})] + \frac{\partial}{\partial z}[gzw(\rho_b + \rho_w)] = -\rho_o\varepsilon, \tag{8}$$

or

$$\frac{\partial E}{\partial t} + \frac{\partial f_E}{\partial x} + \text{vertical redistribution} = -\rho_o\varepsilon, \tag{9}$$

where the horizontal energy flux is

$$f_E = u(\mathrm{KE} + \mathrm{APE} + p_h^w + \rho_o g\eta_H + p_{\mathrm{nh}}), \tag{10}$$

and the rhs of (9) is the energy lost to turbulence, with ε representing the viscous dissipation rate of the kinetic energy of the turbulence.[2] The remaining terms represent vertical transport and are only important for internal redistribution of energy. They disappear in the vertical integral, as $w(z = 0) = 0$ and $w(z = H) \simeq 0$. Since our primary concern here is the lateral energy transport, we neglect the terms labeled "vertical redistribution" in (9).

The horizontal energy flux, f_E, is the sum of nonlinear advection of wave energy (kinetic plus available potential energy) and a pressure–velocity work term, or

$$f_E = uE + up. \tag{11}$$

Our definition differs from that of Venayagamoorthy and Fringer (2005) because of the absence of nonlinear advection and pressure–velocity work terms. These terms involve the background density ρ_b, which is independent of x, and hence do not contribute to lateral transport. Equation (10) also differs from the rigid-lid calculation of Venayagamoorthy and Fringer (2005) in that we have explicitly included the external pressure caused by the disturbance of the free surface. Our observations indicate that $\int_0^H u\, dz \neq 0$, and the net result of the pressure–velocity work term involving $\rho_0 g\eta_H$ is not zero.

The energy flux defined by (10) differs from that for a linear, hydrostatic internal wave, for which $f_E = up_h^w$ (Nash et al. 2005), in two ways. The first is the presence of the nonlinear advection term, uE, and the second is the nonhydrostatic part of the pressure–velocity work term. For a linear wave, it is simply shown (Kundu and Cohen 2004) that

$$\langle up\rangle_{\mathrm{linear}} = c_g\langle E\rangle, \tag{12}$$

where $\langle\rangle = \int_{-\infty}^{\infty}\int_0^H ()\, dz\, dt$ so that

$$\langle f_E\rangle_{\mathrm{linear}} = c_g\langle E\rangle, \tag{13}$$

where c_g is the linear wave group velocity.

Given that a solitary nonlinear internal wave represents a quantity of energy $\langle E\rangle$ confined to a compact region of space that moves with velocity c,[3] it seems appropriate that the resulting energy transport can be described by a flux equal to $c\langle E\rangle$. That is,

[1] Note that $\rho_w(z)$ differs from that defined by Moum and Smyth (2006) as it is referenced to ρ_b and not to $\rho_U(z)$. Moum and Smyth (2006) simply defined $\rho_U(z)$ as the density profile ahead of the wave. This cannot be used as a reference to compute APE.

[2] Equation (8) ignores both the potential propagation loss due to local generation of small-scale but undetected internal waves from the disturbance (Crook 1988) and the energy source associated with the density gradient across the disturbance, as suggested by Henyey and Hoering (1997). We can say nothing about the former and revisit the latter in discussion.

[3] For a nondispersive wave there is no distinction between group and phase velocity. In what follows, we refer to c simply as the wave velocity.

$$\langle f_E \rangle = c\langle E \rangle. \quad (14)$$

Using data obtained from a relatively limited but well-defined and sufficiently well-observed set of individual nonlinear internal waves, we will demonstrate that (14) holds for these observations. We note that (14) is consistent with the following conditions:

- $\rho_0\varepsilon$ can be neglected in (9),
- "vertical redistribution" does not contribute to lateral transport, and
- the wave is steady in a reference frame propagating horizontally at constant speed, c, that is, $\partial/\partial t = -c\partial/\partial x$.

3. Experimental details

The observations discussed here were made from a ship, from a rapidly sampled bottom lander as well as from a full water column mooring (locations shown in the inset of Fig. 2).

From shipboard profiling measurements using the freely falling turbulence profiler Chameleon (Moum et al. 1995), temperature, density, and ε were computed. As well, an optical backscatter probe (880 nm) was deployed together with the microstructure sensors on the nose of Chameleon. An acoustic Doppler current profiler (ADCP; 150 kHz—sampled at 6 s and 4-m vertical bins) and high-frequency echosounder (120 kHz; pinging twice per second) were mounted in the ship's hull. The echosounder provides a means of imaging the flow on fine vertical and temporal/horizontal scales. Even at a profiling rate of one Chameleon profile every 4–5 min, our perspective of the structure of the nonlinear internal waves is aliased.

Over the period from 20 January to 3 February 2003, 12 cross-shelf profiling transects were executed with the ship moving at 1–2 kt from offshore to inshore along the transect line shown on Fig. 2. As well, a profiling time series was conducted near the mooring locations (Fig. 2, inset) over a 36-h period from 30 January to 1 February, while R/V *Revelle* held position to within a few meters using dynamic positioning.

A bottom lander was deployed for the extent of the shipboard observations. Instruments included an upward-looking 300-kHz ADCP (5-s, 1-m ensemble averages recorded from 2 m above the sea bed), and two 5-MHz acoustic Doppler velocimeters (ADVs) sampled at 10 Hz, positioned to either side of the ADCP and 1 m above the bed. A SeaCat (pressure, temperature, and conductivity) was located 1 m above the bed and sampled at 1 Hz. The ADCP and ADV were gimballed to ensure that they remained horizontal. Unfortunately, a malfunction by a data storage device limited data from ADCP and ADVs to a short period from deployment on 20 to 22 January. The SeaCat data extend from 20 January through 3 February.

The shelfbreak mooring included temperature measurements at 1 m above the bed, sampled at 2-min intervals.

4. Observations

Our three different modes of observation (cross-shelf profiling, profiling time series, and lander time series) offer unique perspectives of near-bottom flows. Our objective in this section is to provide a general description of the wave structure with the aid of all of these observational modes.

a. Cross-shelf structure

Typical density structure across the shelf during downwelling is represented by a series of three successive transects at 45°00′N, each separated by 24 h, following and after a period of sustained northward (downwelling favorable) winds. The resultant cross-shore Ekman circulation includes a shoreward near-surface transport and offshore transport near the bottom. A consequence is a distinctive cross-shelf structure in density (represented here as σ_θ; Fig. 3). Light fluid near the surface is concentrated at the inshore boundary, enhancing stratification there (this is seen most clearly in the right panel of Fig. 1). Denser fluid near the bottom is driven offshore. In between, at midshelf, the water column is weakly or neutrally stratified. This is a consequence of the combination of cross-shelf circulation and intense wintertime surface forcing (A. Perlin et al. 2006, unpublished manuscript).

Offshore of the shelf break (nominally 200 m) the positions of isopycnals at depths greater than the mixed layer depth are controlled by mesoscale motions and/or the internal tide; this is independent of the downwelling circulation. In each example shown in Fig. 3, the isopycnals indicate the presence of an abrupt near-bottom front over the shelf (at 18 km in the first transect, 15 km in the second and 12 km in the third).[4] Two common aspects of these fronts are high optical backscatter above the seafloor and high ε at the leading edges. High optical backscatter at the seafloor indicates

[4] Although we have no observations between these transects, there is no reason to think that this is a progression of the same feature. The small translation speeds inferred from Fig. 3 are 1/10 of what we would expect from accompanying analysis.

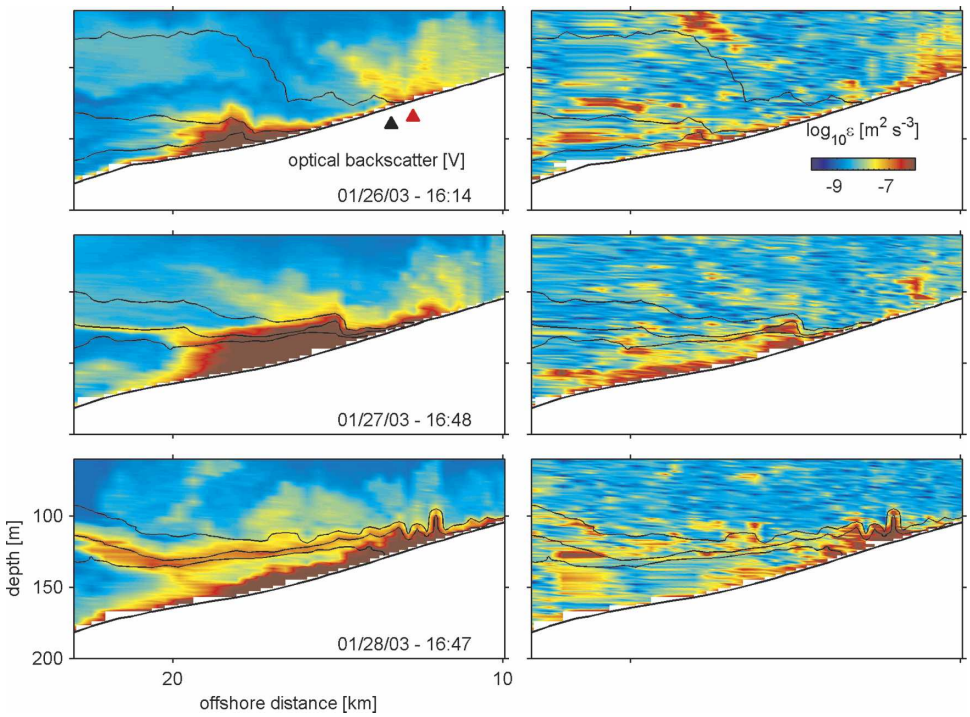

FIG. 3. Cross-shelf structure of isopycnals (black lines; 0.5 kg m^{-3} spacing; the same isopycnals are shown in each panel): (left) optical backscatter (red high; blue low) and (right) turbulence dissipation rate for three crossings of the shelf at 45°N on three successive days in January 2003. The time at the beginning of each crossing (beginning at the offshore end of the transect) is shown in the left panels. Locations of bottom lander (red triangle) and shelfbreak mooring (black triangle) are noted in the top left panel. These are restricted views of our measurements. The complete cross-shelf distribution of isopycnals for the third transect is shown in Fig. 1. Note that the upper 50 m of the water column have been omitted from these images.

resuspension of sediments, likely caused by the elevated turbulence there.

The nature of these fronts differs between transects. The second is much sharper (and more turbulent) than the first; the third is clearly wavelike. At the head of the front in the third example appears to be a train of propagating internal solitary waves of elevation discussed by Klymak and Moum (2003).

b. Profiling time series

In our 36-h profiling time series, a sequence of similar (though far from identical) near-bottom structures are revealed (denoted by the inverted triangles atop Fig. 4). These fronts are accompanied by vertical displacements of near-bottom isopycnals by 25–30 m over periods of about 5 min [corresponding to vertical velocities of $O(0.1\ \mathrm{m\ s^{-1}})$]. They are spaced in time by 9 h 15 min, 14 h 20 min, and 8 h 10 min, successively, suggesting no simple correspondence with the dominant M_2 tide (the barotropic component of which dominates variations in sea surface height shown in the upper panel of Fig. 4). Like the fronts depicted in Fig. 3, each front in Fig. 4 is accompanied by high optical backscatter and high ε.

These profiling data were obtained during a period of northward flow that is strongly modulated in amplitude (third panel, Fig. 4). The cross-shelf component of the flow is modulated in both amplitude and direction (second panel, Fig. 4), apparently a result of the internal tide. Unfortunately, current measurements from shipboard ADCP do not include the bottom 20 m and our bottom lander had expired by the time of this profiling time series. Given these shortcomings, together with the short record length, it is difficult to assess correspondences between the density fronts and currents.

Finer details of the structure at the front are provided by shipboard echosounder measurements aided by the Chameleon profiles. Figure 5 shows the evolution of a scattering layer that defines the complex structure of the final front observed in the 36-h series in Fig. 4. We presume that the scattering layer, which is initially located 1–5 m above the bottom, is a deep zooplankton layer. This layer is raised 25 m by the first undulation of the bore and an additional 10 m by the next undulation.

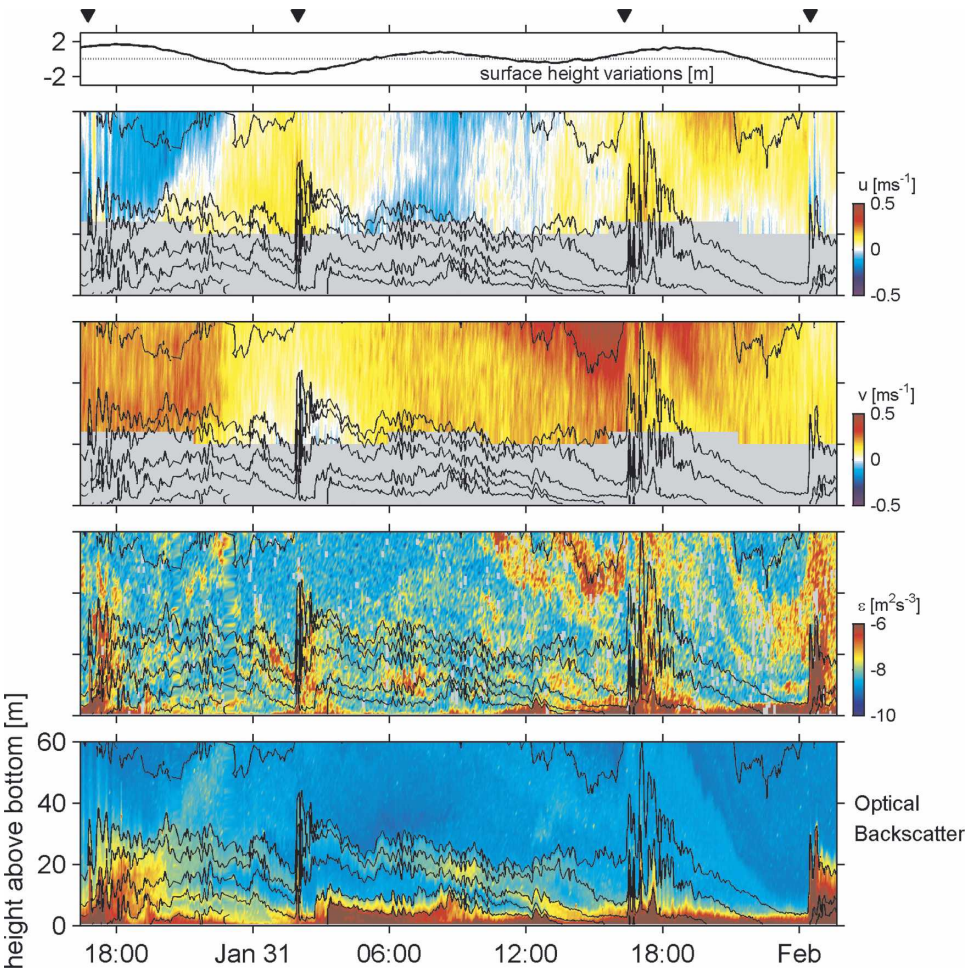

FIG. 4. Time series of profiling measurements at the location shown in Fig. 2. Water depth is 124 m. (top) The variations in surface height as measured by a pressure sensor on the lander ADCP. (second from top) Cross-shelf currents (U—red $>$ 0, eastward). (third from top) Alongshelf currents (V—red $>$ 0, northward). (fourth from top) Turbulence dissipation rate (ε). (bottom) Optical backscatter. Density contours are at intervals of 0.2 kg m^{-3}. The occurrence of each bore is noted by the black triangles above the top panel. The final density front coincides with the image shown in Fig. 5.

Following this are a sequence of smaller undulations. The scattering layer remained 20 m above the bed more than 1 h following the passage of the initial front.

One aspect of the near-bottom scattering response shown in Fig. 5 seems to be consistent with most of the fronts we observed. Bright scatterers appear from the bottom following passage of the initial density front. This is possibly the emergence of bottom dwellers in response to the changing environmental conditions carried along with the fronts.

Contours of σ_θ plotted on the echosounder image confirm that the vertical displacement of the principal scattering layer reflects the vertical displacement of nearby isopycnals (Fig. 5). The density structure further reveals the continual near-bottom density increase behind the front (the near-bottom density increase of 0.5 kg m^{-3} is seen in the difference between initial and final density profiles in Fig. 5). In detail, isopycnals indicate a bulbous structure at the leading edge of the densest fluid (note the black isopycnals just after 0100 UTC). This is expected at the head of a gravity current flowing over the bottom as fluid flow above the bottom is reduced to zero at the seafloor [as depicted in the laboratory results of Britter and Simpson (1978), e.g., their Fig. 1a].

The structure of the density fronts at 1-m height corresponding to our profiling time series, from measurements at each of the three locations shown in Fig. 2, is seen in Fig. 6. Measurements of temperature and conductivity at the lander were restricted to a single measurement at 1-m height. As the nearest conductivity measurement from the bottom was at 10-m height at

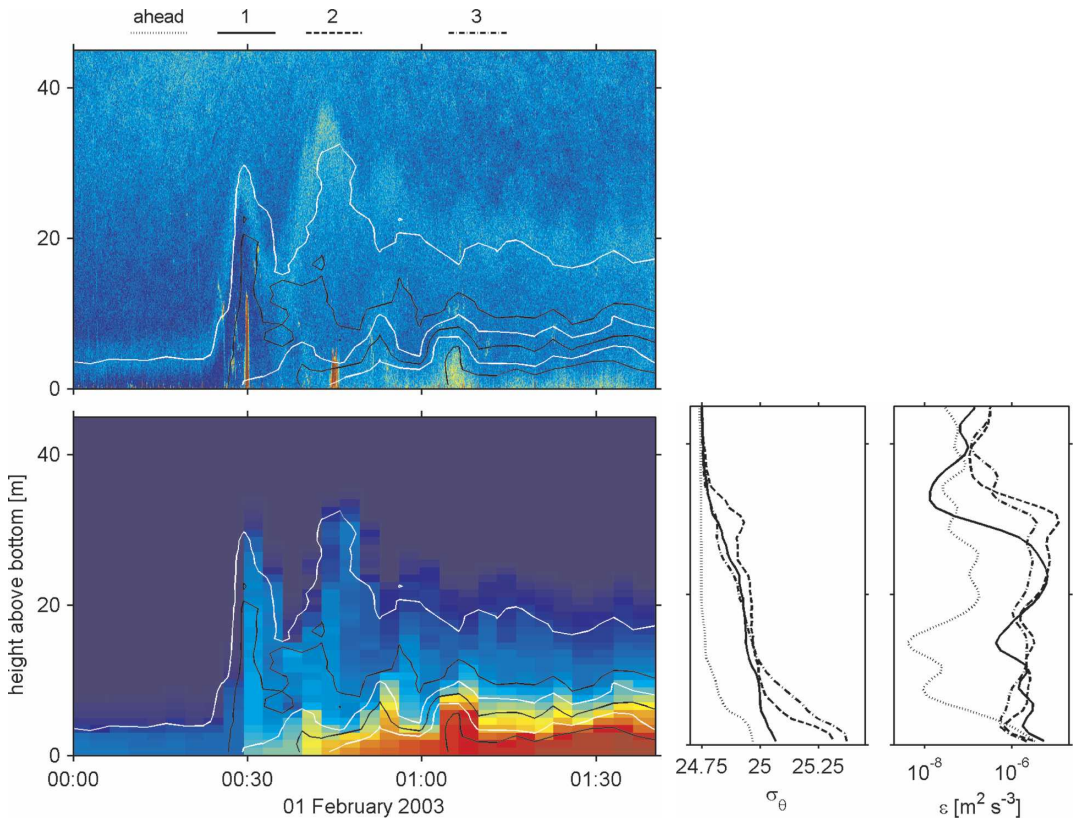

FIG. 5. Expanded plot of the final density front shown in Fig. 4. (top) Acoustic image of internal bore with σ_θ contours at 0.1 kg m^{-3} intervals. (bottom) Image plot of σ_θ with contours at 0.1 kg m^{-3} intervals. To the right of the bottom panel are vertical profiles of σ_θ and ε averaged (four–seven Chameleon profiles) at the times shown above the top panel.

the shelfbreak mooring, our only complete comparison is potential temperature. The bores propagate principally onshore, so the 653 m east–west separation between lander and shelfbreak mooring provides a basis for estimating the speeds of the fronts (Moum and Smyth 2006). The signature of each bore is unique and evolves between the locations of lander and shelfbreak mooring. In fact, the only example that is unambiguously defined at both locations is the final bore. The inset in the upper panel of Fig. 6 shows the time of arrival of the front at these locations to differ by 1 h, giving an estimate of the frontal propagation speed as 0.18 m s^{-1}.

c. *Lander time series*

Unfortunately, we have no velocity measurements from our lander that coincide with the 36-h profiling time series shown in Figs. 4–6. However, the lander was fully operational for the first 52 h of its deployment and the perspective offered is unique. The data are also sufficiently detailed to permit an assessment of the energy flux. During the 52-h deployment, six fronts passed the lander, traveling almost directly onshore (as determined from the direction of currents in the bore at 1-m height). Their spacing in time was 2 h 50 min, 8 h 15 min, 5 h 25 min, 8 h 45 min, and 23 h 15 min.

A 22-h record from the bottom lander shows the first four of these fronts (Fig. 7). Both the rate of and the total density increase across each front differs considerably. At each front is an abrupt velocity pulse followed by a series of pulses. Each of these pulses is bottom trapped and directed toward the shore, but the vertical displacements and separations between pulses varied considerably. The initial velocity pulse of fronts 1, 3, and 4 coincides with the initial density increase. In front 2 the initial velocity pulse occurs before (ahead of) the large density increase; it does, however, coincide with a smaller, local density increase (Figs. 8, 9).

The density and velocity structure of the final front is not typical. In this final front the first velocity pulse coincided with a pulse of dense fluid at 1-m height. The initial velocity pulse was detected by the ADV at 1-m height, but the following pulses had velocity maxima more than 20 m above the bottom and no velocity sig-

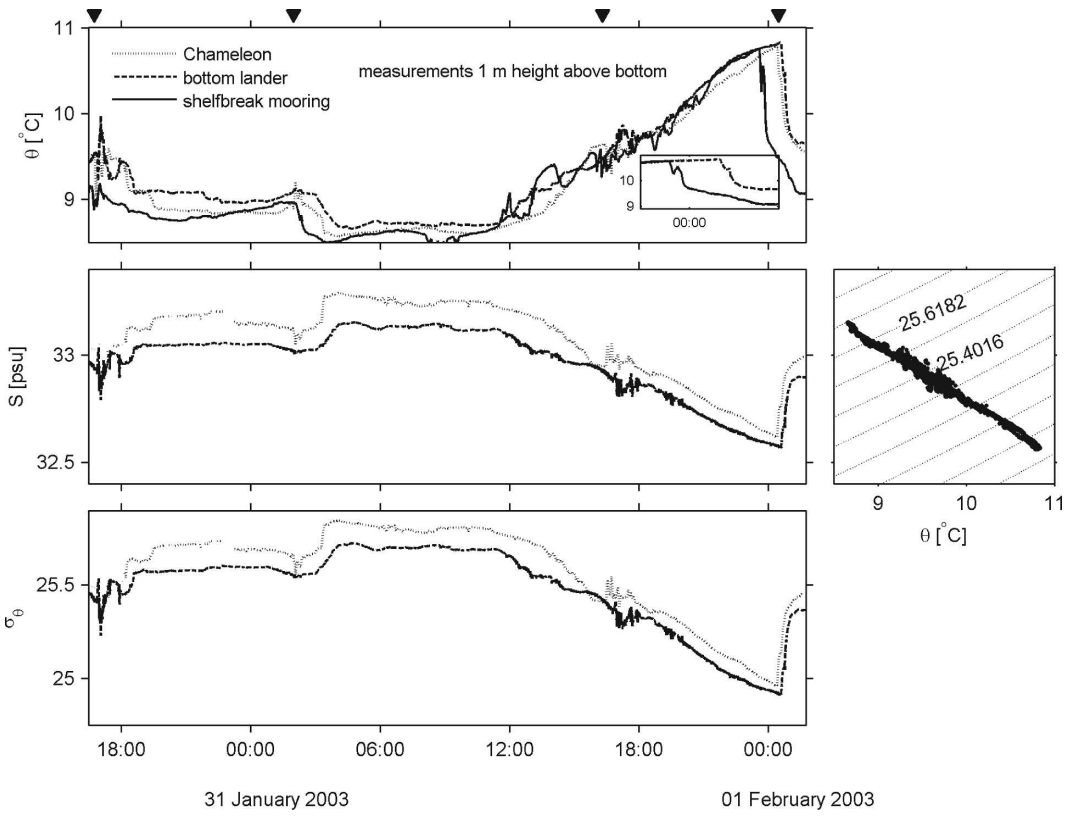

FIG. 6. (top) Time series of temperature 1 m above the seafloor for the period of the profiling time series in Fig. 4 at each of the locations shown in the expanded plot of Fig. 2. The inset shows the detail of the front associated with the bore depicted in Fig. 5. (middle), (bottom) Salinity and σ_θ 1 m above the seafloor from the bottom lander and Chameleon. The time of occurrence of each bore at the location of the Chameleon profiling time series is denoted by the inverted triangle at the top of the figure. To the right is the θ–S relationship at 1-m height for the duration of the series; lines of constant σ_θ are dashed.

nature at 1-m height. It is known that large-amplitude midwater column internal waves can be excited by an intrusive gravity current (Mehta et al. 2002). This may help to explain the lack of a bottom signature.

While no two fronts were the same, an example shows the salient features (Fig. 8). This front was accompanied by a density increase of 0.15 kg m^{-3}, which occurred over a period of about 1.5 h. The flow at 1-m height was composed of an oscillatory component of 0.4 m s^{-1} peak-to-peak plus a mean component of $\simeq$0.15 m s^{-1} during the passage of the density front. The direction of both the mean component of the flow and the pulses was due east. Eleven pulses are clearly visible in the record, each with the distinctive vertical velocity signature of an elevation wave (upward ahead and downward behind each wave). The first two pulses were separated by about 15 min and the rest appeared with a 10-min separation. The onshore component of the flow extended almost 50 m above the bottom for the first three pulses.

The strong shear at the crest of the pulses is seen in the detail of the structure of the first pulse of Fig. 8 (expanded in Fig. 9).[5] The shear is also intense at the bottom where the fluid velocity $\rightarrow 0$. The reduction of velocity above the crest and at the bottom means that there is a maximum in between, as seen in the vertical profile averaged at the crest in Fig. 9.

The internal structure of the wave pulse is revealed in some detail when the phase speed is subtracted from the local fluid velocity.[6] The phase speed estimate used here is the second-order phase speed determined by solution of the Korteweg–deVries (KdV) equation (Gear and Grimshaw 1983); solutions for these particular examples are described by Moum and Smyth (2006). Removal of the phase speed provides a depiction of the fluid motion in the frame of reference of the wave (Fig. 10; here, $c = 0.48$ m s^{-1}). This two-dimensional per-

[5] This particular wave is used as an instructional example in the energy calculations to follow.

[6] We consider the pulse to be a wave to justify use of a phase speed.

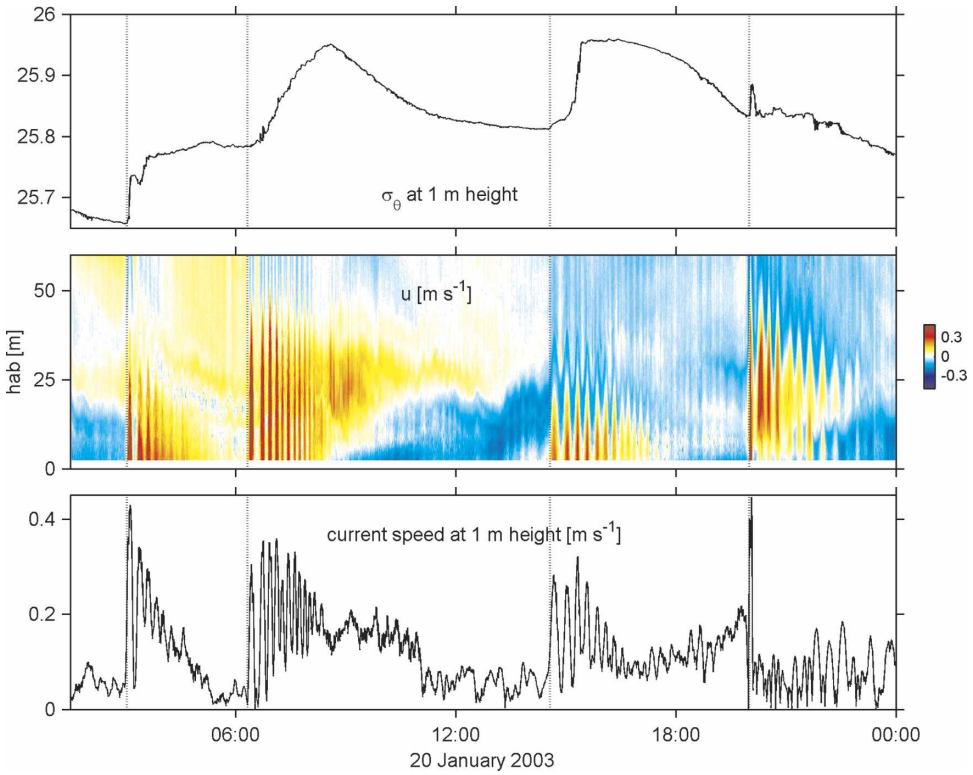

FIG. 7. Time series of measurements from bottom lander: (top) σ_θ at 1-m height above the bottom; (middle) horizontal component of velocity (30-s ADCP averages) in the direction of wave propagation (due east); and (bottom) current speed at 1-m height from ADV measurement. Vertical dashed lines indicate the arrival times of leading waves in each group as determined from the velocity records.

spective suggests circulation in the x–z plane similar to what we might expect if trapped cores exist within the wave (Lamb 2003; Klymak and Moum 2003). Fluid parcels within the wave core with velocities $> c$ are part of an internal recirculation that forms closed streamlines that move at speed c. However, the flow is not two-dimensional and some of this velocity structure is associated with three-dimensional flow, presumably an indication of turbulence and instabilities within the wave.

d. Turbulence

The dissipation rate of turbulence kinetic energy was computed from ADV measurements 1 m above the bottom (see the appendix). Intense turbulence was observed beneath and following the crest of the first wave (Fig. 9). The trailing edges of the first four waves in Fig. 8 were progressively more turbulent, after which the fluid passing the lander was continuously turbulent, and ε was 100 times as great as before the wave passage. Because $N^2 \simeq 3 \times 10^{-4}$ s^{-2} (Moum and Smyth 2006, their Fig. 3), corresponding to a buoyancy time scale $2\pi/N \simeq 400$ s, which governs the decay of unforced, stratified turbulence (Smyth et al. 1997), the elevated turbulence following wave passage must be continuously generated.

The vertical structure of enhanced turbulence behind the front is indicated by the set of averaged ε profiles shown in Fig. 5. At 10-m height, the increase in ε was approximately a factor of 100, from 10^{-8} to 10^{-6} across the front. Behind the front ε was relatively constant over the bottom 30 m.

The bottom stress, τ_b, was estimated using wall-layer scaling in the bottom boundary layer applied to the ADV measurement 1 m above the bottom; $u_* = (\varepsilon\kappa z)^{1/3}$ and $\tau_b = \rho u_*^2$ (Perlin et al. 2005b). Peak values of $\tau_b \approx 1$ N m^{-2} coincide with peak speeds in the wave pulses. This demonstrates the intense and immediate interaction of the pulses with the bottom. Such high stresses at the periphery of the wave core represent a primary distinction between near-bottom waves of elevation and near-surface waves of depression that do not interact with a solid boundary.

e. Summary of observations

Cross-shelf transects clearly show high ε and high turbidity at sharp, near-bottom fronts (Fig. 3). As they

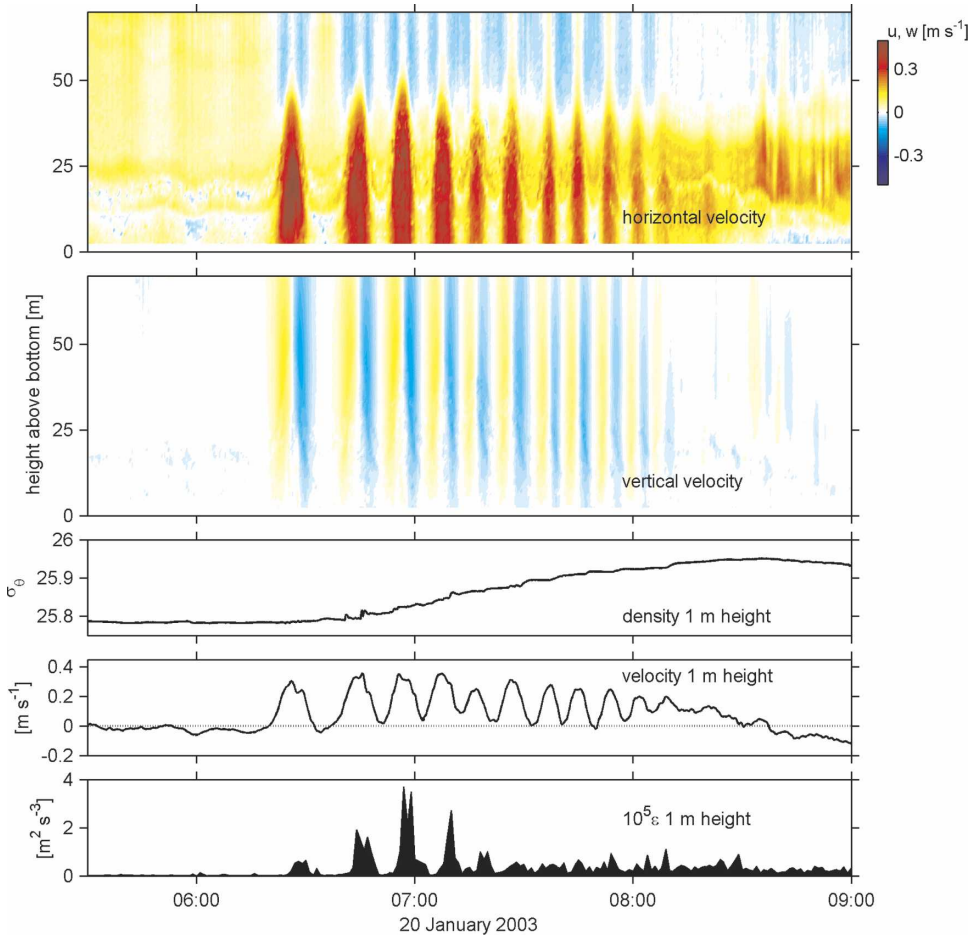

FIG. 8. Time series of measurements from bottom lander. (top) Horizontal component of velocity (30-s ADCP averages) in the direction of wave propagation (due east); (second from top) vertical component of velocity; (third from top) σ_θ at 1-m height above the bottom; (fourth from top) horizontal component of velocity (2-s averaged ADV) in the direction of wave propagation at 1-m height; (bottom) ε (1-min averages) computed from the vertical component of the ADV-measured velocities at 1-m height (as described in the appendix).

approach the shore, these fronts have been observed to evolve into a series of solitary-like waves (Klymak and Moum 2003).

Our profiling time series (Fig. 4) offers a somewhat different perspective. In particular, the detailed imaging provided by high-frequency acoustics suggests that the structure of the fronts is similar to what has been referred to as internal undular bores in atmospheric and laboratory flows. The structure outlined in Fig. 5 is similar to that observed by upward-looking echosounder images in northern Australia (Fig. 3 in Christie et al. 1981), by downward-looking echosounder images showing depressions of scattering layers near the sea surface in Knight Inlet, British Columbia, Canada [by D. Farmer and reproduced by Simpson (1997) as Fig. 7.16], and by dye in a laboratory experiment to replicate some of the properties of the geophysical examples (Simpson 1997, Fig. 13.5). In each of these cases, the signature is attributed to a combination of undular internal bore and internal solitary waves. Rottman and Simpson (1989) showed how these can be created in the laboratory at the leading edge of a gravity current and, indeed, density measurements shown in Fig. 5 demonstrate the signature of a gravity current behind the leading edge of the bore.

A third perspective is found in the detailed, near-bottom velocity profiling measurements from our lander time series. Here, the leading edges of the density fronts are observed to coincide with a velocity signature that would appear as undulations in either isopycnals or acoustic scattering layers. However, the velocity signature is clearly pulselike (or solitary wavelike) in that individual velocity pulses (or wave cores) are distinct from each other and proceed with signifi-

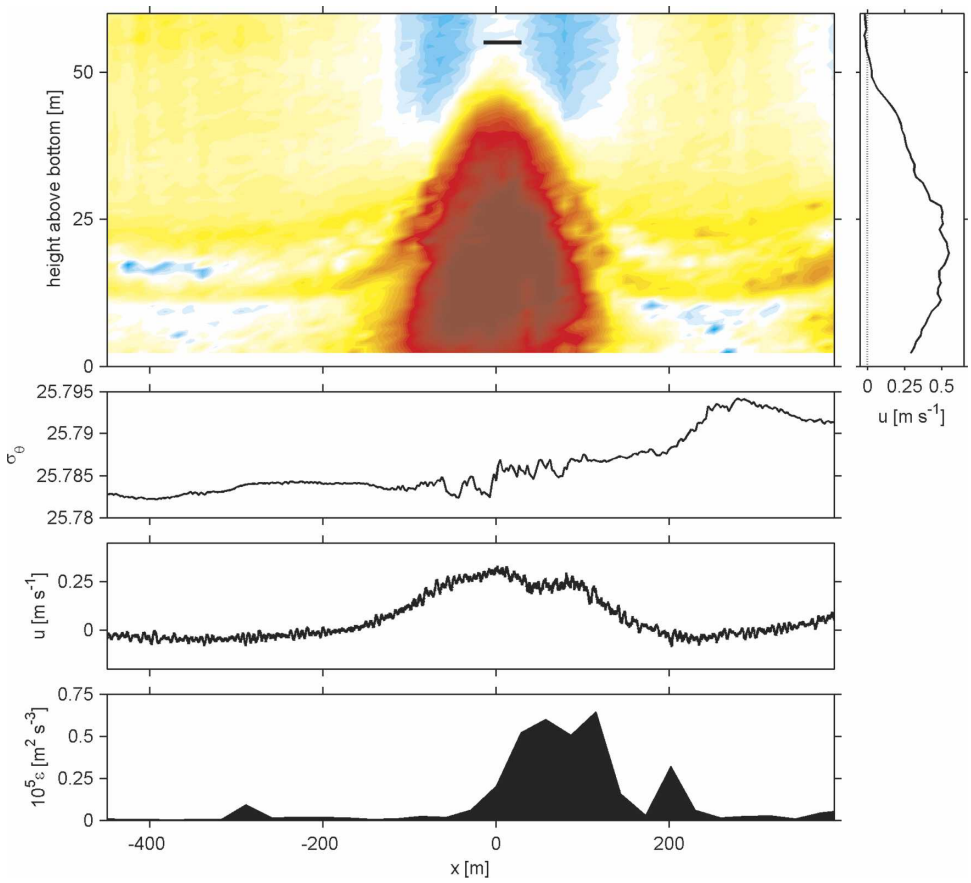

FIG. 9. Time series of measurements from bottom lander translated to a spatial series via $x = c_1(t - t_0)$. (top) Horizontal component of velocity (5-s ADCP averages) in the direction of wave propagation; (second from top) σ_θ at 1-m height above the bottom; (third from top) horizontal component of velocity (0.5-s averaged ADV) in the direction of wave propagation at 1-m height; and (bottom) ε (1-min averages) at 1-m height. To the right of the top panel is a vertical profile of horizontal velocity averaged over the interval indicated by the horizontal black line at $x = 0$.

cantly greater speed than the remainder of the fluid behind the density fronts. Moum and Smyth (2006) have treated these as trains of propagating waves. Whether the appearance of the waves ahead of the fronts is analogous to wave fission from a density current (Nash and Moum 2005) cannot be addressed from this set of measurements.

These observations are typical of those involving geophysical fluid flows in that they demonstrate a combination of traits that have each been clearly defined theoretically and in the laboratory but are difficult to separate in geophysical observations. The features that we observe have aspects that are both wavelike (i.e., symmetric perturbations about the disturbance) and borelike (i.e., associated with sloping isopycnals and horizontal pressure gradients). Henyey and Hoering (1997) coined the term *solibore* to represent the combination of features. For the remainder of this analysis, we consider the wavelike components of the flow in isolation from the background gradients. The objective is to define the range of magnitudes of kinetic and potential energy contained within the waves and to assess how the energy is transported by them. The borelike aspects of the energetics are addressed by E. Shroyer et al. (2006, unpublished manuscript). Ultimately, we must consider the interplay between the waves and the density fronts in which they are observed, as these fronts apply a pressure gradient and represent a source of potential energy (Henyey and Hoering 1997).

5. Energetics

The data obtained using the bottom lander provide a detailed measurement of the velocity field in the waves. In particular, the leading three waves of each of the four wave groups depicted in Fig. 8 have velocities

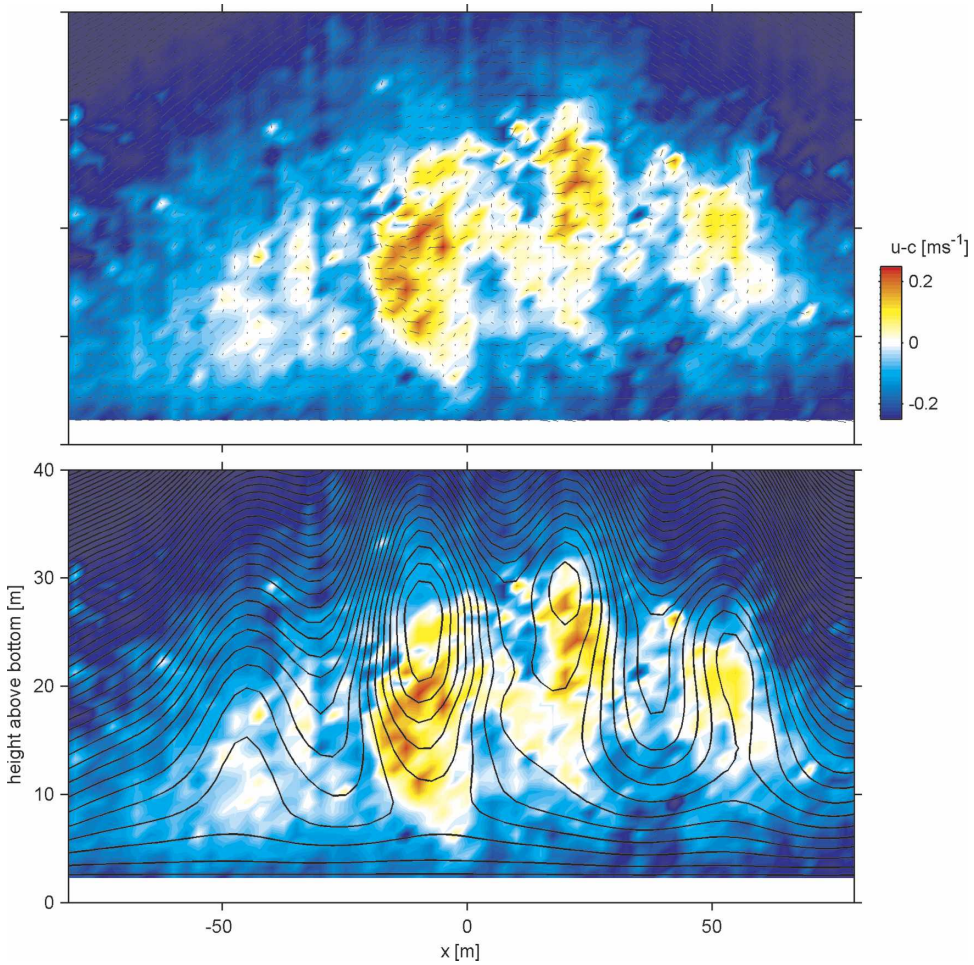

FIG. 10. (top) Velocity vectors ($x-z$ plane; 5-s averages) in a reference frame moving with the wave. The image plot represents the horizontal velocity component; warm colors indicate $u > c$. (bottom) Streamlines computed from velocity vectors are added to the image plot; they are averaged over 10 m in both the vertical and horizontal dimensions.

that are large relative to both the background flows and also to any borelike component of the flow. Moum and Smyth (2006) used the velocity fields as observed from the bottom lander to reconstruct the density and pressure field of each of these 12 waves. With the assumption that the waves are inviscid, two-dimensional, and propagate without change in shape with known speed and direction, isopycnals parallel streamlines. Using a background density profile, isopycnals were mapped to streamlines computed from the velocity measurements as described by Moum and Smyth.

Our purpose here is to quantify the total wave energy, the rate at which it is transported, and to identify the role of individual terms in the energy transport as they appear in (10). Identical computations are applied to each of the 12 clearly defined waves examined by Moum and Smyth (2006). From a time series, we cannot differentiate between the time dependence of E and the spatial divergence of f_E, so we cannot make a direct assessment of (9). Instead, we assess f_E, E, and $\rho_0\varepsilon$ independently, find that $\rho_0\varepsilon$ is small over short propagation ranges, and compare f_E and E via (14); that is, $\langle f_E \rangle = c\langle E \rangle$.

a. *KE* and *APE*

As an example calculation we show details of the first wave of the second group of waves depicted in Fig. 7, shown in detail in Fig. 9.[7] The energy density (kJ m^{-3}) is shown in Fig. 11; KE is positive definite. APE is positive in the vicinity of the wave (isopycnals are

[7] This is the pedagogical example shown by Moum and Smyth (2006); we return to this example throughout our discussion of the energetics.

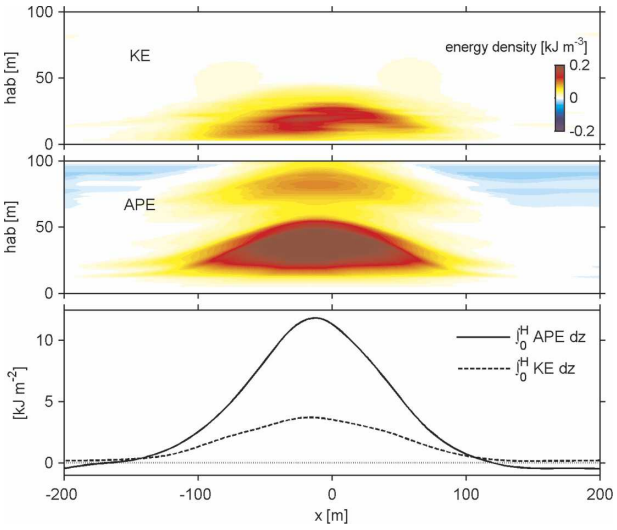

FIG. 11. (top) KE density through the wave shown in Fig. 9. (middle) APE density. (bottom) Vertically integrated energies.

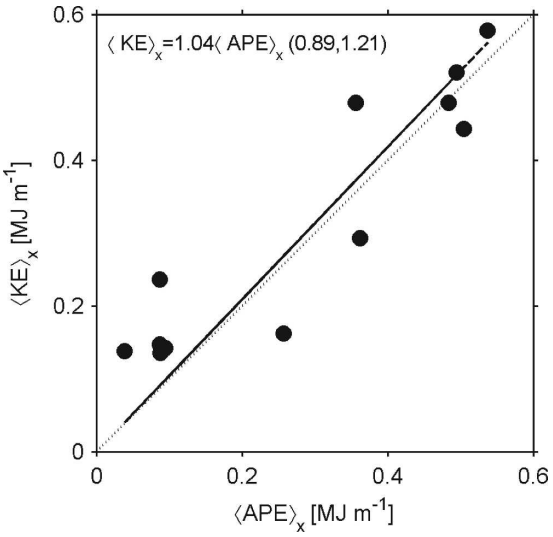

FIG. 12. $\langle \mathrm{KE} \rangle_x$ vs $\langle \mathrm{APE} \rangle_x$. A neutral regression fit (with 95% confidence intervals) is indicated.

raised) and slightly negative elsewhere, a necessary consequence of the definition of ρ_b. This is reflected in the vertical integral of APE.

In the vicinity of the wave core, at least where KE is nonzero, the vertical integral of APE is about 4 times that of KE. However, when integrated over the domain ($\langle\rangle_x = \int_{-\infty}^{\infty} \int_0^H () \, dz \, dx = \int_{-\infty}^{\infty} \int_0^H ()c \, dz \, dt$), estimates of central tendency indicate that $\langle KE \rangle_x \simeq \langle APE \rangle_x$. Note that the negative APE, remote from the wave core, contributes significantly to the time integral.

The ratio $\langle KE \rangle_x / \langle APE \rangle_x$ displays considerable scatter (Fig. 12); this is particularly so among the low-energy cases. Neutral regression indicates $\langle \mathrm{KE} \rangle_x = 1.04$ (0.89, 1.21) times $\langle \mathrm{APE} \rangle_x$, with 95% confidence limits in parentheses.

b. Energy flux

We first consider the three pressure–velocity flux (Fig. 13). As p_{nh} is mostly negative (Moum and Smyth 2006, Fig. 9), so is the energy flux associated with it. The effect of the negative surface displacement above an elevation wave is similarly to cause a negative energy flux. The fact that the vertical integral is nonzero while $\rho_0 g \eta_H$ is independent of z is because $\int_0^H u \, dz \neq 0$. This suggests a net onshore transport of fluid in the waves. How this is resolved through continuity is beyond our ability to determine with the present measurements. However, there is a variable background flow (Fig. 7) that we have not removed because of considerable ambiguity in exactly how to do this. Note that this differs from the linear wave assumption (Kunze et al. 2002) and from that used for the rigid-lid simulation of Venayagamoorthy and Fringer (2005). The hydrostatic pressure–velocity flux is > 0, and larger in magnitude than the sum of the other two terms. As a consequence, the net effect of pressure–work is a net positive (onshore, in the direction of wave propagation) energy transport (solid line in bottom panel of Fig. 14). The net pressure–work transport is of the same sign but smaller than the nonlinear advection term uE in the example shown in Fig. 14. Neutral regression yields $\langle uE \rangle = 2.01$ (1.29, 3.28) times $\langle up \rangle$.

Depth-dependent time integrals through the waves provide a complementary view of the vertical structure of individual flux terms and of the net wave flux (Fig. 15). These flux profiles show consistent features com-

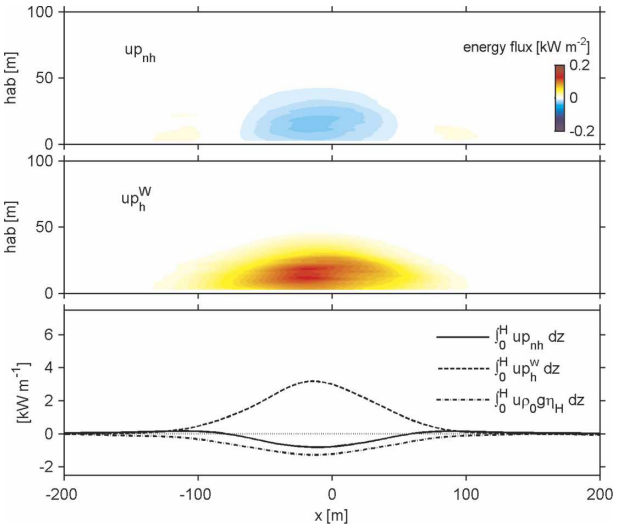

FIG. 13. (top),(middle) Components of the pressure–velocity energy flux. (bottom) Their vertical integrals.

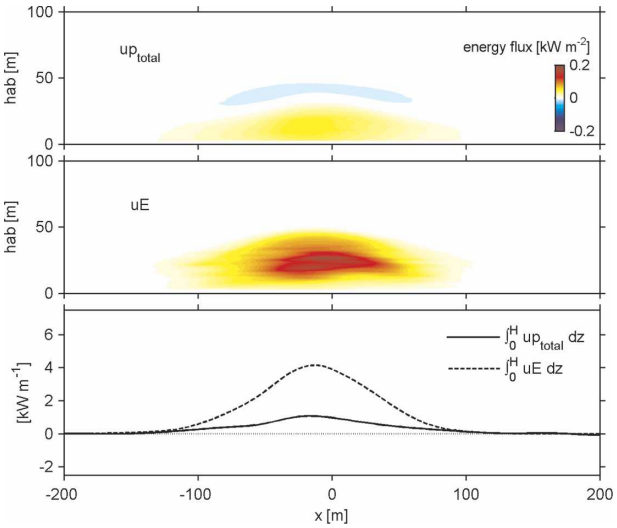

FIG. 14. (top),(middle) Components of the energy flux. Here up_{total} is the sum of the terms shown in Fig. 13. (bottom) Their vertical integrals.

mon to all of the waves. Notably, the vertical distributions of advective and pressure–velocity terms differ significantly. The effect of the pressure–work transport term is to carry the energy close to the bottom. Dominated by the advection of APE, the nonlinear advection term acts farther away from the bottom.

c. Dissipative losses

Estimates of the energy dissipated via turbulence in the wave cores are derived from vertical profiles (Figs. 4, 5) as well as from measurements at 1-m height above the seafloor from lander-based observations (Figs. 8, 9, and A1). The profiles in Fig. 5 suggest that, in the wave cores, ε is relatively uniform with height above the bottom and very close to its magnitude at 1-m height (Fig. A2). A scale estimate of 3×10^{-6} m^{-2} s^{-3} seems like a reasonable upper bound to an average value in the wave cores. Integrated over the wave core, $\langle \rho_0 \varepsilon \rangle_x$ is $O(1\text{–}10)$ W m^{-1}. This is compared to the total wave energy, which is $O(10^6)$ J m^{-1} (Fig. 12). The ratio $\langle E \rangle_x / \langle \rho_0 \varepsilon \rangle_x$ represents a dissipative decay time scale, which is $O(10^5\text{–}10^6)$ s, or 1–10 days. If we take a typical wave period to be 500 s (e.g., Fig. 8), this is equivalent to several hundred to several thousand wave periods. Or, at $c = 0.5$ m s^{-1}, a distance of tens to hundreds of kilometers. This implies that, over short propagation ranges, we can neglect $\rho_0 \varepsilon$ in (9). However, it is quite likely that these waves propagate at least hundreds of wavelengths, and the integral effect of dissipative losses must be considered over these longer propagation ranges [this has been recently demonstrated by Moum et al. (2007)]. For our purpose, we consider (14) as a test of our estimates of f_E and E.

We note here that we have not considered the energy required to propagate up the sloping shelf, which will appear as an energy sink in the long propagation problem. Evaluating this term is complicated by our incomplete knowledge of the mass transport by the waves. It is also complicated by the finite extent of the near-bottom waveguide. In fact, this waveguide may be

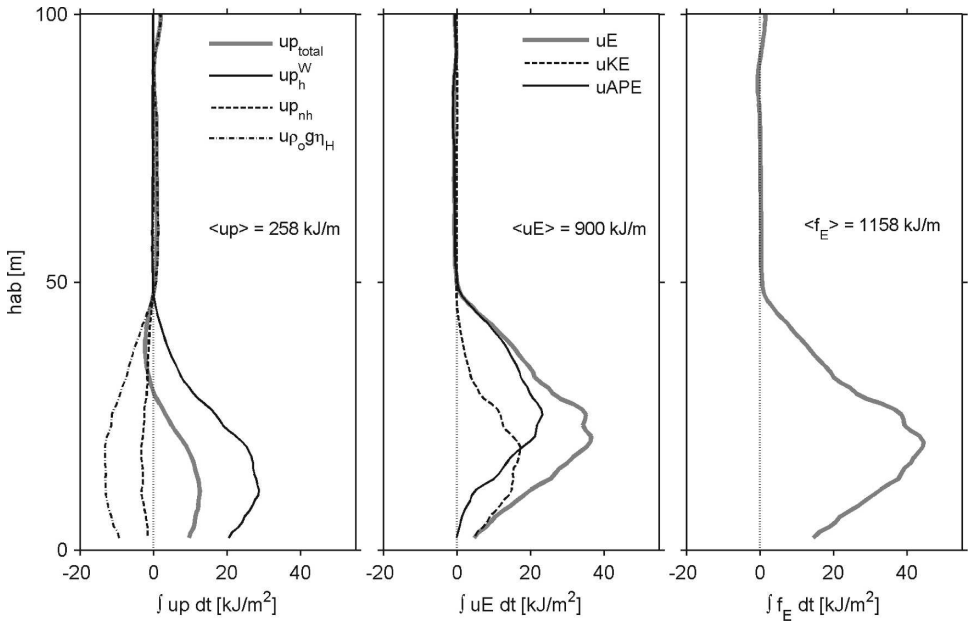

FIG. 15. Vertical profiles of fluxes integrated over the example wave shown in Fig. 9. The total transport is indicated as the vertical integral of the profiles.

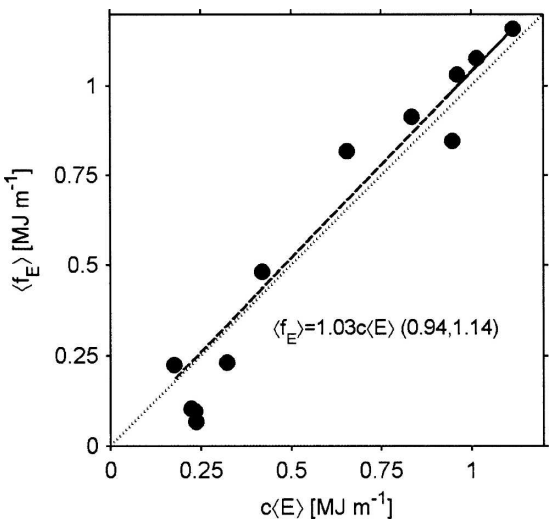

FIG. 16. Comparison of $\langle f_E \rangle$ vs $c\langle E \rangle$. A neutral regression fit (with 95% confidence intervals) is indicated.

partly due to the cumulative contributions of past wave trains that have transported dense fluid up the shelf.

d. Relating flux to energy

Direct comparison of $\langle f_E \rangle$ to $c\langle E \rangle$ reveals that they are nearly equal (Fig. 16).[8] We have found it difficult to evaluate the uncertainty in these estimates, but it is doubtful that Fig. 16 suggests anything other than $\langle f_E \rangle = c\langle E \rangle$. The mean value of $\langle f_E \rangle / c\langle E \rangle$ is 0.88 with standard deviation 0.34 and standard error of the mean 0.10. The median value of this ratio is 1.04 and the neutral regression results in $\langle f_E \rangle = 1.03$ (0.94, 1.14) times $c\langle E \rangle$.

6. Discussion

Analogies for the observed flows exist in atmospheric and laboratory flows. The "morning glory" in northern Australia has been considered a classic form of an internal undular bore in the atmosphere (Clarke et al. 1981). It has also been described in terms of solitary waves (Christie et al. 1981). The coincidence of an undular bore and gravity current has been noted in the case of a thunderstorm outflow (Marks 1974) and depicted schematically by Rottman and Simpson (1989). The purpose of the experiments of Rottman and Simpson was to replicate the conditions for the generation of these atmospheric phenomena. Generation of intermittent turbulence resulting from gravity currents and solitary waves in the nocturnal atmospheric boundary layer has been observed by Sun et al. (2004).

The structure of near-bottom nonlinear internal waves must differ from that of waves propagating in a near-surface waveguide; the requirement that $u = 0$ at the bottom means that there is an injection of vorticity into the wave core of one sign from below and of the other sign from above. A close look at Fig. 9 indicates an evolution of the near-bottom shear as the wave passed. A sharp reduction occurred at or following the increase in turbulence past the wave crest. This suggests that the strong interaction with the bottom may result in rapid diffusion of wave core momentum, introducing asymmetry across the wave.

In the case of surface-trapped waves, the wave-induced surface stress is minimal and therefore the injection of vorticity from the surface must also be small. In surface-trapped waves it may be that the primary source of turbulence is from shear instabilities at the bottom interface (Moum et al. 2003).

Although there is an elevation of turbulence across the wave trains (Fig. 8), the larger turbulence bursts in individual waves are relatively short lived (Fig. A1), at least in the leading waves. Turbulence appears at 1-m height within the wave cores and invariably disappears abruptly as the wave cores pass. The decay appears to be significantly shorter than the local buoyancy time scale (Smyth et al. 1997), indicating that it is not the stratification that attenuates the turbulence. This suggests that the turbulent fluid generated within the waves is trapped in and transported by the waves, not left behind to decay. It is consistent with the notion of "trapped cores" carried in the wave without contact with the ambient water (Lamb 2003), evidence of acoustic scatterers trapped in wave cores (Klymak and Moum 2003) and supported by Fig. 10.

There are several ways in which these near-bottom flows may impact shelf transport. High bed stresses act to resuspend seafloor particulate matter into the water column. These particles are raised high into the water column (many tens of meters) by vertical wave motions and thence irreversibly mixed by energetic turbulence. At the same time, we note that the direction of fluid transport by the waves must be in the direction of the energy transport (onshore). This is in the direction opposite to that of the Ekman transport in the bottom boundary layer beneath the northward flow that characterizes the shelf circulation during downwelling. Taken together, these motions may effect a significant vertical and cross-shelf transport, which has not been previously been considered. So far as we know, none of these factors are incorporated into modern coastal circulation models.

Osborne and Burch (1980) assumed equipartition of kinetic and potential energies in their description of

[8] Note that our definitions of integrals results in $c\langle E \rangle = \langle E \rangle_x$.

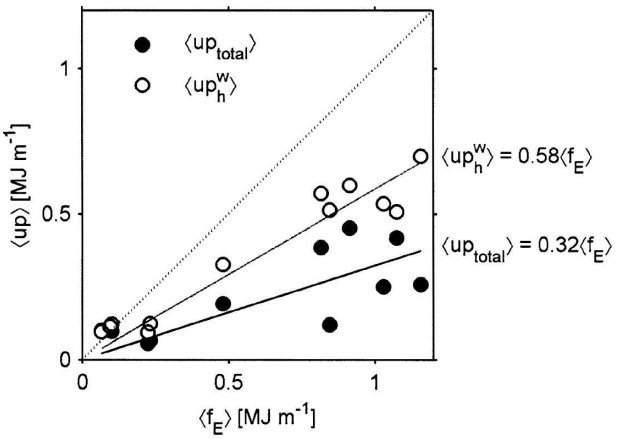

FIG. 17. $\langle f_E \rangle$ vs $\langle up \rangle$. Solid dots represent the total pressure–velocity energy flux. Open circles include only the hydrostatic part of the pressure–velocity energy flux.

solitons in the Andaman Sea. They stated, but did not demonstrate, that equipartition holds "approximately" for KdV solitons in a two-layer fluid. For geophysical solitary waves, however, the weakly nonlinear limit of KdV theory provides only an approximate description. Nonlinearity is generally not weak, and KdV theory can provide no guidance in this case. Here, we have suggested $\langle KE \rangle \simeq \langle APE \rangle$. For comparison, Klymak and Moum (2003) estimated $\langle \mathrm{KE} \rangle / \langle \mathrm{APE} \rangle = 1.5$ from a sample of three bottom-trapped waves with energy levels at the low end of those discussed here; this is a revision of the analysis presented in the original paper. Klymak et al. (2006) determined $\langle \mathrm{KE} \rangle / \langle \mathrm{APE} \rangle = 1.4$ for a single large-amplitude, surface-trapped wave in the South China Sea with energy level four orders of magnitude greater than the waves analyzed here.

For internal waves that can be linearized, the energy flux is due solely to pressure–velocity work, the only pressure contribution being the internal hydrostatic component, p_h^w (Nash et al. 2005). It is straightforward to theoretically relate this to $c_g \langle E \rangle_{\mathrm{linear}}$ (Kundu and Cohen 2004), and this has been verified experimentally (Alford and Zhao 2007). The present observations indicate that an analogous result holds for finite-amplitude, nondispersive waves with propagation speed c: $\langle f_E \rangle = c \langle E \rangle$.

For nonlinear internal waves, the energy flux includes both a nonlinear advection term and a nonhydrostatic pressure–velocity work term that do not appear in the linear wave flux formulation. Yet the linear wave flux formulation has been applied to nonlinear waves (Chang et al. 2006). Since $\langle uE \rangle$ is such a large component of $\langle f_E \rangle$ (from Fig. 17, $\langle uE \rangle \simeq (\frac{2}{3}) \langle f_E \rangle$), this cannot be justified. It is significant that a larger fraction of the total energy flux is falsely represented by $\langle up_h^w \rangle$ (than $\langle up_{\mathrm{total}} \rangle$) because the sum of the nonhydrostatic plus surface displacement contributions to the pressure–velocity flux counters that due to p_h^w (as represented by the open circles and gray lines in Fig. 17). By neglecting the opposing contributions to the pressure–velocity flux and the nonlinear advection term, a closer approximation of the wave flux is achieved, albeit for the wrong reasons. Even then, this represents only 60% of the true value.

The cumulative energy transported by many wave trains is estimated by extrapolation from our small set of observations. We note that, while four wave trains were observed on 20 January (shown in Fig. 7), almost an entire day passed until the next wave train was observed. Our estimates of wave energy transport (neglecting the borelike part) suggests $\Sigma \langle f_E \rangle \simeq 20$ MJ m^{-1}, and that this occurred over a 48-h period. This, in turn, implies an onshore energy transport by the waves alone of about 100 W m^{-1}. Independent estimates of onshore energy transport indicate a similar energy flux by the M_2 internal tide (at 45°N: G. Avicola 2005, personal communication).

Other analyses indicate that most of the energy at M_2 transported across the shelf in 120-m water depth during upwelling when stratification is significant across the shelf propagates shoreward through 80-m water depth to 50-m depth (120, 80, and 50 m were the nominal depths of moorings at 45°N; G. Avicola 2005, personal communication). On the other hand, during the downwelling experiment of January 2003, when a large portion of the shelf was unstratified, the proportion of M_2 energy reaching 50 m was reduced by a factor of 4. Is it possible that most of the energy in the M_2 frequency band at the shelf break went into nonlinear internal waves? Or that, at least the internal tide is an efficient generator of nonlinear internal waves at this time of year? Certainly the lack of stratification at midshelf (Fig. 1) indicates the problems inherent in internal wave propagation to the inner shelf.

The timing of the arrival of wave groups at the observing site is not phase locked to M_2. However, it is possible that M_2 forcing is disguised by differential propagation speeds as stratification varies between shelf break and observational site (thus altering c) and that M_2 forcing is itself modulated by the variability in the location of density interfaces near the shelf break caused by the mesoscale circulation.

In assessing the energetics of the waves we have reconstructed density from streamlines, which has produced nearly symmetric density structure across the waves. However, the waves (or wave groups) are clearly associated with a larger-scale density front and

the structure of density is not generally symmetric across the waves.

Our use of a symmetric density structure means that we have not attempted to address the more subtle problem posed by Henyey and Hoering (1997); that is, whether the potential energy difference across individual waves or wave groups is in balance with the energy dissipated by turbulence. It is clear, though, from our analysis of individual waves passing a point in space that, over short propagation ranges, dissipative losses are not important. This is at least consistent with observations of nonlinear internal waves of depression propagating in deep water in the South China Sea (Klymak et al. 2006). But over long propagation ranges, say hundreds of wavelengths, turbulence losses should be important if our measurements of ε in these wave cores is representative. In the case of nonlinear internal waves of depression propagating more than 100 wavelengths over a shoaling shelf, Moum et al. (2007) found the approximate balance $dE/dt = -\rho_0\varepsilon$.

7. Summary

Near-bottom flows over the Oregon shelf during winter downwelling exhibit characteristics of a gravity current, internal bore, and solitary wave. Groups of wavelike pulses with high-velocity cores ($u \simeq 0.5$ m s^{-1}) were observed at the leading edges of density fronts. These are associated with high bed stresses and internal turbulence that forms rapidly and disappears as individual high-velocity wave cores pass.

Evaluation of nonlinear internal wave kinetic energy, available potential energy, and energy flux indicates the following:

- energy is roughly equipartitioned between kinetic and potential,

$$\langle \mathrm{KE} \rangle \simeq \langle \mathrm{APE} \rangle;$$

- the energy flux is simply related to the total wave energy by the wave speed,

$$\langle f_E \rangle \simeq c\langle E \rangle;$$

- the pressure–velocity energy flux includes significant contribution from both nohydrostatic pressure and surface displacement, which, since they are of opposite sign to the hydrostatic pressure–velocity flux, reduces the total contribution of pressure–velocity work to the nonlinear wave energy flux; and
- nonlinear advection of energy is a significant component of the energy flux and is a direct measure of the wave's nonlinearity. For the waves we have observed,

$$\langle uE \rangle \simeq 2\langle up \rangle.$$

The first two properties are consistent with linear waves. The latter two are unique to nonlinear internal waves.

Acknowledgments. This work was funded by the National Science Foundation (9907854, 0453140) and by the Office of Naval Research. We acknowledge the assistance of Mike Neeley-Brown, Ray Kreth, and Greig Thompson. The bottom temperature record from the shelfbreak mooring was kindly provided by Murray Levine, Tim Boyd, and Mike Kosro. We are grateful to captain and crew of R/V *Revelle* for their contributions to the success of this experiment.

APPENDIX

Turbulence Measurements

A detailed account of our bottom lander ADV turbulence measurements reveals some interesting characteristics of the near-bottom turbulence induced by passing nonlinear internal waves. A comparison of ε estimates from these measurements and those from our turbulence profiler indicates some consistency between two different periods of nonlinear internal wave-induced turbulence.

A spectrogram of the cross-shore component of velocity recorded by an ADV at 1-m height with low-passed current speed overplotted is shown in Fig. A1. Spectra were computed over 2048 points (204.8 s). The spectrogram indicates one of the complications of quantifying turbulence from rapidly sampled velocity records in shallow water. In 124-m water depth, the velocity signature of wind waves (2–5 s) at the bottom is negligible, but that of 12+ s swell is not. The most energetic components of this signal are due to two swell components: one constant at about 12 s, the other varying in period from about 22 to 15 s over the record shown. The longer period swell component also increased in energy over the record.

Turbulence in the spectrogram record (Fig. A1) is identified by the broadband signal at frequencies greater than that of the swell. Turbulence associated with the wave pulses dominates the record. The rapid onset of turbulence as the velocity pulses pass indicates either rapid generation of turbulence within each pulse or advection of turbulence by the wave pulses. While this is an important distinction to make, we do not have enough information from these data to tell the difference.

The problem of interpreting the high-frequency component of a spectrum when inertial subrange turbulence is advected by a random wave field past a point

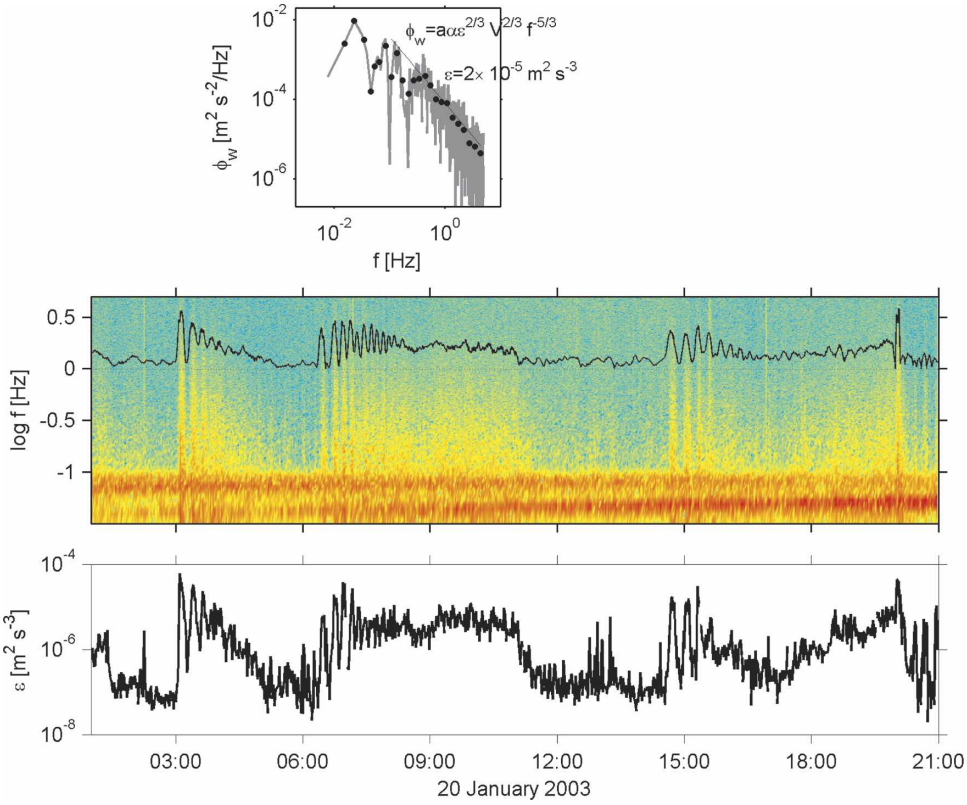

FIG. A1. (middle) Spectrogram of cross-shore velocity measured by ADV on bottom lander. Individual spectra were computed over 2048 points of the 10-Hz-sampled signal (204.8 s). Ordinate is $\log_{10}$ of frequency (Hz); abscissa is time. Color indicates $\log_{10}$ of spectral amplitude (m^2 s^{-2} Hz^{-1}). The black line across the image plot is the current speed shown in Fig. 7; this is scaled to the ordinate axis in units of meters per second. (top) An example spectrum of vertical velocity with an inertial subrange scaled by measured dissipation and current speed (V); $a = 12/55$ and $\alpha = 1.5$. (bottom) The time series of ε derived from the spectra.

measurement of velocity was addressed by Lumley and Terray (1983) in order to interpret observations under much more extreme conditions in terms of the relative contribution of wave orbital velocities, very near the surface beneath wind waves in Lake Ontario. This was refined by Trowbridge and Elgar (2001) to apply to bottom ADV measurements in the surf zone. We use Trowbridge and Elgar's method here to define the turbulence dissipation rate, ε, from our bottom ADV measurements. The full record of ε computed over 204.8-s intervals is shown in Fig. A1.

Unfortunately, we do not have coincident turbulence records from the profiler and bottom lander. A comparison of ε determined from Chameleon measurements 1 m above the bottom and that determined from the ADV on the bottom lander, at different periods but which each include nonlinear internal waves, is shown in histogram form (Fig. A2). These data represent measurements from the entire records shown in Figs. 4 and A1. Each dataset includes four density fronts with sequences of wave pulses as well as bottom boundary layer turbulence of other origin. We note that the two distributions in Fig. A2 are similar. Mean and median values of the two distributions differ by about 50%, the lander values being larger (lander mean $= 2.6 \times 10^{-6}$ m^2 s^{-3}; lander median $= 8.4 \times 10^{-7}$ m^2 s^{-3}). Since the profile measurements underresolve the time variability of the turbulence in the wave pulses,[A1] we might expect that the lander series samples more of the infrequent large values of ε, which could explain the difference in the distributions at high values of ε. Alternatively, this difference could be a real feature of the turbulence between these two periods. The differences at low values of ε are explained by the differing noise levels of the two calculations (the lander ADV measurements

[A1] This is because the duration of the pulses is about 10 min while our profiling rate in this water depth was about one per 4 min.

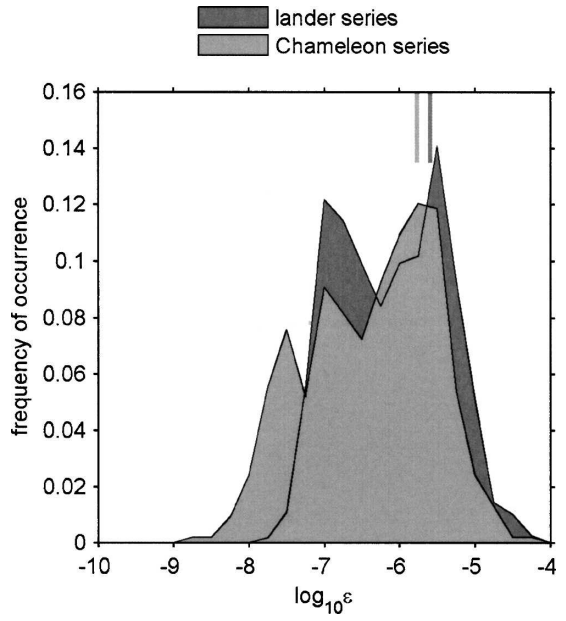

FIG. A2. Comparison of ε estimates at 1-m height determined from the Chameleon profile measurements shown in Fig. 4 and from the bottom lander ADV measurements shown in Fig. A1. Median values of each distribution are indicated by the vertical lines at the top of the figure. The lander median is greater by about 50%.

demonstrated a noise level that is about 10 times as great).

REFERENCES

Alford, M. H., and Z. Zhao, 2007: Global patterns of low-mode internal-wave propagation. Part II: Group velocity. *J. Phys. Oceanogr.,* **37,** 1849–1858.

Britter, R. E., and J. E. Simpson, 1978: Experiments on the dynamics of a gravity current head. *J. Fluid Mech.,* **88,** 223–240.

Chang, M.-H., R.-C. Lein, T. Y. Tang, E. A. D'Asaro, and Y. J. Yang, 2006: Energy flux of nonlinear internal waves in northern South China Sea. *Geophys. Res. Lett.,* **33,** L03607, doi:10.1029/2005GL025196.

Christie, D. R., K. J. Muirhead, and R. H. Clarke, 1981: Solitary waves in the lower atmosphere. *Nature,* **293,** 46–49.

Clarke, R. H., R. K. Smith, and D. G. Reid, 1981: The morning glory of the Gulf of Carpenteria: An atmospheric undular bore. *Mon. Wea. Rev.,* **109,** 1726–1750.

Crook, N. A., 1988: Trapping of low-level internal gravity waves. *J. Atmos. Sci.,* **45,** 1533–1541.

Gear, J., and R. Grimshaw, 1983: A second order theory for solitary waves in shallow fluids. *Phys. Fluids,* **26,** 14–29.

Hebert, D., 1988: The available potential energy of an isolated feature. *J. Geophys. Res.,* **93,** 556–564.

Helfrich, K. R., and W. K. Melville, 2006: Long nonlinear internal waves. *Annu. Rev. Fluid Mech.,* **38,** 395–425.

Henyey, F. S., and A. Hoering, 1997: Energetics of borelike internal waves. *J. Geophys. Res.,* **102,** 3323–3330.

Holloway, P. E., 1987: Internal hydraulic jumps and solitons at a shelf break region on the Australian North West shelf. *J. Geophys. Res.,* **92,** 5405–5416.

Hosegood, P., and H. van Haren, 2003: Near-bed solibores over the continental slope in the Faeroe-Shetland Channel. *Deep-Sea Res.,* **51,** 2943–2971.

Huyer, A., R. L. Smith, and E. J. C. Sobey, 1978: Seasonal differences in low-frequency current fluctuations over the Oregon continental shelf. *J. Geophys. Res.,* **83,** 5077–5089.

Klymak, J. M., and J. N. Moum, 2003: Internal solitary waves of elevation advancing on a shoaling shelf. *Geophys. Res. Lett.,* **30,** 2045, doi:10.1029/2003GL017706.

——, R. Pinkel, C.-T. Liu, A. K. Liu, and L. David, 2006: Prototypical solitons in the South China Sea. *Geophys. Res. Lett.,* **33,** L11607, doi:10.1029/2006GL025932.

Kundu, P. K., and I. M. Cohen, 2004: *Fluid Mechanics.* 3d ed. Elsevier Academic, 759 pp.

Kunze, E., L. K. Rosenfeld, G. S. Carter, and M. C. Gregg, 2002: Internal waves in Monterey Submarine Canyon. *J. Phys. Oceanogr.,* **32,** 1890–1913.

Lamb, K. G., 2003: Shoaling solitary internal waves: On a criterion for the formation of waves with trapped cores. *J. Fluid Mech.,* **478,** 81–100.

——, 2007: Energy and pseudoenergy flux in the internal wave field generated by tidal flow over topography. *Cont. Shelf Res.,* **27,** 1208–1232.

Lien, R.-C., T. Y. Tang, M. H. Chang, and E. A. D'Asaro, 2005: Energy of nonlinear internal waves in the South China Sea. *Geophys. Res. Lett.,* **32,** L05615, doi:10.1029/2004GL022012.

Lumley, J. L., and E. A. Terray, 1983: Kinematics of turbulence convected by a random wave field. *J. Phys. Oceanogr.,* **13,** 2000–2007.

MacKinnon, J. A., and M. C. Gregg, 2003: Shear and baroclinic energy flux on the summer New England shelf. *J. Phys. Oceanogr.,* **33,** 1462–1475.

Marks, J., 1974: Acoustic radar investigations of boundary layer phenomena. NASA Contractor Rep. CR-2432, 65 pp.

Mehta, A. P., B. R. Sutherland, and P. J. Kyba, 2002: Interfacial gravity currents. II. Wave excitation. *Phys. Fluids,* **14,** 3558–3569.

Moum, J. N., and W. D. Smyth, 2006: The pressure disturbance of a nonlinear internal wave train. *J. Fluid Mech.,* **558,** 153–177.

——, M. C. Gregg, R. C. Lien, and M. Carr, 1995: Comparison of turbulence kinetic energy dissipation rate estimates from two ocean microstructure profilers. *J. Atmos. Oceanic Technol.,* **12,** 346–366.

——, D. M. Farmer, W. D. Smyth, L. Armi, and S. Vagle, 2003: Structure and generation of turbulence at interfaces strained by internal solitary waves propagating shoreward over the continental shelf. *J. Phys. Oceanogr.,* **33,** 2093–2112.

——, ——, E. L. Shroyer, W. D. Smyth, and L. Armi, 2007: Dissipative losses in nonlinear internal waves propagating across the continental shelf. *J. Phys. Oceanogr.,* **37,** 1989–1995.

Nash, J. D., and J. N. Moum, 2005: River plumes as a source of large amplitude internal waves in the ocean. *Nature,* **437,** 400–403.

——, M. H. Alford, and E. Kunze, 2005: On estimating internal wave energy fluxes in the ocean. *J. Atmos. Oceanic Technol.,* **22,** 1551–1570.

Osborne, A. R., and T. L. Burch, 1980: Internal solitons in Andaman Sea. *Science,* **208,** 451–460.

Perlin, A., J. N. Moum, and J. M. Klymak, 2005a: Response of the bottom boundary layer over the continental shelf to varia-

tions in alongshore winds. *J. Geophys. Res.,* **110,** C10S09, doi:10.1029/2004JC002500.

——, ——, ——, M. D. Levine, T. Boyd, and P. M. Kosro, 2005b: A modified law-of-the-wall to describe velocity profiles in the bottom boundary layer. *J. Geophys. Res.,* **110,** C10S10, doi:10.1029/2004JC002310.

Pinkel, R., 2000: Internal solitary waves in the warm pool of the western equatorial pacific. *J. Phys. Oceanogr.,* **30,** 2906–2926.

Reid, R. O., B. A. Elliott, and D. B. Olson, 1981: Available potential energy: A clarification. *J. Phys. Oceanogr.,* **11,** 15–29.

Rottman, J. W., and J. E. Simpson, 1989: The formation of internal bores in the atmosphere: A laboratory model. *Quart. J. Roy. Meteor. Soc.,* **115,** 941–963.

Sandstrom, H., and J. A. Elliott, 1984: Internal tide and solitons on the Scotian Shelf. *J. Geophys. Res.,* **89,** 6419–6426.

Scotti, A., R. C. Beardsley, and R. Butman, 2006: On the interpretation of energy and energy fluxes of nonlinear internal waves: An example from Massachusetts Bay. *J. Fluid Mech.,* **561,** 103–112.

Simpson, J. E., 1997: *Gravity Currents in the Environment and Laboratory.* 2d ed. Cambridge University Press, 244 pp.

Smith, R. K., N. Crook, and G. Roff, 1982: The Morning Glory: An extraordinary atmospheric undular bore. *Quart. J. Roy. Meteor. Soc.,* **108,** 937–956.

Smyth, W. D., P. O. Zavialov, and J. N. Moum, 1997: Decay of turbulence in the upper ocean following sudden isolation from surface forcing. *J. Phys. Oceanogr.,* **27,** 810–822.

Sun, J., and Coauthors, 2004: Atmospheric disturbances that generate intermittent turbulence in nocturnal boundary layers. *Bound.-Layer Meteor.,* **110,** 255–279.

Trowbridge, J. H., and S. Elgar, 2001: Turbulence measurements in the surf zone. *J. Phys. Oceanogr.,* **31,** 2403–2417.

Venayagamoorthy, S. K., and O. B. Fringer, 2005: Nonhydrostatic and nonlinear contributions to the energy flux budget in nonlinear internal waves. *Geophys. Res. Lett.,* **32,** L15603, doi:10.1029/2005GL023432.

Winters, K. B., P. N. Lombard, J. J. Riley, and E. A. D'Asaro, 1995: Available potential energy and mixing in density-stratified fluids. *J. Fluid Mech.,* **289,** 115–128.